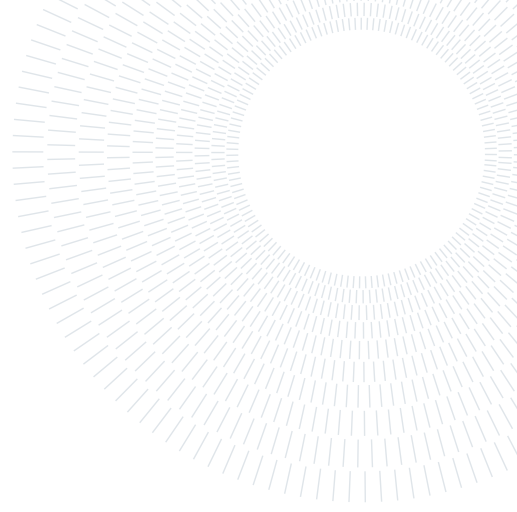




POLITECNICO
MILANO 1863

SCUOLA DI INGEGNERIA INDUSTRIALE
E DELL'INFORMAZIONE



Class Assignments 5

COMPUTATIONAL TECHNIQUES FOR THERMOCHEMICAL PROPULSION (051176)

Samuele Orsenigo, 10735389

Prof.:

Federico Piscaglia

Academic year:

2024-2025

1. Introduction

This report documents the setup and outcomes of the final phase of a university project, focusing on the simulation of a three-dimensional combustor (Figure 1). The study investigates the combustion of *n*-Heptane with air, where the fuel is introduced into the computational domain as Lagrangian particles. The simulation does not account for fluid-wall interactions, simplifying the physical model while maintaining relevance to practical applications.

The primary aim of this project is to build upon and refine the computational and analytical skills acquired throughout the course. This involves extracting both physically meaningful and technically valuable insights from the simulation results. Advanced post-processing techniques and statistical analyses are employed to ensure efficient data handling, minimizing storage requirements while maximizing the clarity and utility of the extracted information.

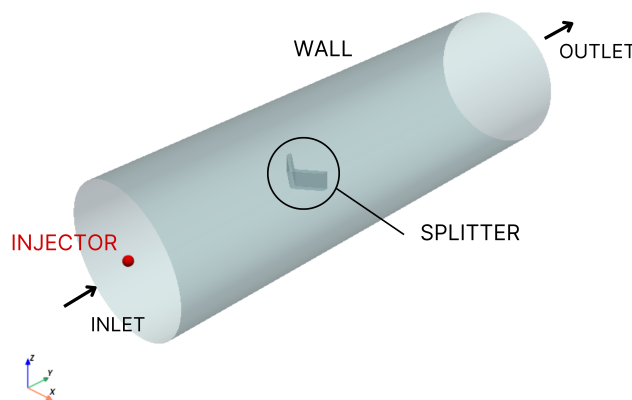


Figure 1: 3D combustor geometry and problem setup

2. Set Up of the Problem

This section presents the problem setup. This report consolidates the procedures previously developed in other assignments; however, for the sake of completeness, all steps are thoroughly explained and reiterated.

The simulations were performed on a computer with the following hardware specifications:

- **CPU:** 13th Gen Intel Core i5-1335U (1.3 GHz, 6 physical cores, 12 threads)
- **RAM:** 16 GB
- **GPU:** Intel® Iris® Xe Graphics (integrated)

2.1. Mesh

The STL file was provided by the professor. The object is enclosed within a cylindrical domain with a radius of 120 mm and a length of 800 mm. Inside this domain, a "V"-shaped splitter is positioned. As illustrated in Figure 1, the mesh patches are divided into inlet, outlet, and wall. The "wall" category encompasses all surfaces considered solid boundaries, including the cylinder walls and the splitter. Based on the assignment requirements and the computational power available, the maximum allowable number of mesh cells was set to 380,000. Various test on the mesh was preliminary conduct, due to near delivery deadline, discrete computational power and some problem encounter we decided to reduce the mesh cell to speed up the computation.

2.1.1 Mesh Setup and Results

The OpenFOAM utility `snappyHexMesh` was employed to generate a mesh that aligns with the physical problem while ensuring accurate and reliable results within the defined computational constraints.

A castellated mesh approach was utilized to achieve higher resolution in critical regions, particularly:

- Flame front and Injection area
- Splitter for flow and parcel interaction
- Wake region behind the splitter (for vortex resolution)

Three cylindrical refinement zones were applied to ensure adequate resolution in these regions, detailed in Table 1.

Table 1: Refinement Levels in Key Regions

Refinement Zone	Point 1 (x,y,z)	Point 2 (x,y,z)	Radius (m)	Refinement Level
Combustor Region	(0, -0.2995, 0)	(0, 0.05, 0)	0.03	3
Splitter Cylinder	(0, -0.05, 0)	(0, 0.1, 0)	0.05	3
Post-Splitter	(0, 0.1, 0)	(0, 0.45, 0)	0.08	2

During the mesh design process, it was observed that reducing the wall refinement level significantly decreased the total cell count while maintaining sufficient accuracy. This was deemed an acceptable compromise, given that film layer modeling was not included, reducing the need for excessive wall refinement.

Furthermore, five boundary layers were applied to the walls, while three inflatable layers were added to the splitter surface.

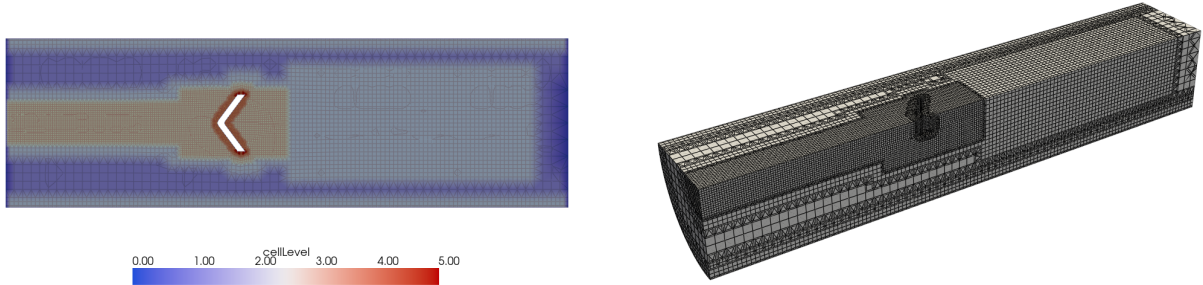
The final mesh comprises approximately 260,000 cells, representing a good balance between accuracy and computational efficiency.

Figures 2a and 2b illustrate the characteristics of the computational mesh. Figure 2a shows the refinement levels, emphasizing structured resolution in critical regions of interest, as describe in Table 1. Figure 2b presents a quarter of the mesh to highlight the axisymmetric mesh definition.

2.1.2 Mesh Analysis

The mesh was analyzed using the `checkMesh` utility, producing the results summarized in Table 2.

The generated mesh presents several positive aspects. It is predominantly hexahedral, with approximately 89% of the cells being structured, which ensures good numerical stability and accuracy. The aspect ratio remains within an acceptable range, with a maximum value of 10.48, reducing the risk of numerical errors due to highly



(a) Mesh refinement levels highlighting key areas of interest.

(b) Quarter-section view of the mesh showing axisymmetric details.

Figure 2: Visualization of the computational mesh with refinement levels and axisymmetric details.

Table 2: Mesh Quality Metrics

Metric	Value
Number of cells	260,284
Hexahedral cells	231,985
Polyhedral cells	19,515
Maximum aspect ratio	10.4796 (OK)
Minimum face area	$6.12 \times 10^{-8} \text{ m}^2$
Maximum face area	$5.81 \times 10^{-4} \text{ m}^2$
Minimum cell volume	$2.01 \times 10^{-11} \text{ m}^3$
Maximum cell volume	$1.36 \times 10^{-5} \text{ m}^3$
Non-orthogonality	Max = 64.9659, Avg = 11.1986 (OK)
Maximum skewness	1.48622 (OK)

stretched elements. Additionally, the skewness value of 1.486 is well within the recommended limits, indicating a well-shaped mesh. The distribution of cell sizes is also reasonable, with a clear distinction between minimum and maximum values, ensuring a proper resolution of flow features.

However, some aspects could be improved. The maximum non-orthogonality reaches 64.97, which is relatively high and may require the use of additional non-orthogonal correction terms in the solver to maintain accuracy. The wide variation in cell volumes, ranging from $2.01 \times 10^{-11} \text{ m}^3$ to $1.36 \times 10^{-5} \text{ m}^3$, could lead to numerical issues, especially in regions with steep gradients. Additionally, the presence of 19,515 polyhedral cells, although beneficial for geometry adaptation, might influence convergence behavior and computational efficiency.

Overall, the mesh is of good quality, but minor refinements, particularly in highly non-orthogonal regions, could enhance its performance in simulations.

2.2. Numerics

The simulation comprises two stages: the cold case (precursor simulation) and the hot case. Both simulations utilize the same mesh described in subsection 2.1. The cold case operates without combustion or Lagrangian particle tracking and serves to initialize the flow field for the subsequent hot case.

2.2.1 Hot Case

Simulation Setup: The hot case simulation starts at $t = 0.08 \text{ s}$, with a maximum Courant number of 0.3 and the `adjustTimeStep` option enabled to ensure accurate resolution of the complex combustion dynamics. The solver employed is `multicomponentFluid`, using a PIMPLE algorithm with three correctors and two outer

correctors. Relaxation factors are applied for numerical stability: $p = 0.3$, $U = 0.7$, and $h, k, \epsilon = 0.5$.

Numerical Schemes: The time integration is performed using the Euler scheme, while the finite volume (FV) schemes are configured as detailed in Table 3.

Scheme Type	Field/Term	Scheme
ddtSchemes	default	Euler
gradSchemes	default	Gauss linear
divSchemes	default div(phi,U) div(phi,Yi_h) div(phi,K) div(phid,p) div(phi,epsilon) div(phi,k) div(((rho*nuEff)*dev2(T(grad(U)))))	none Gauss limitedLinearV 1 Gauss limitedLinear 1 Gauss limitedLinear 1 Gauss limitedLinear 1 Gauss limitedLinear 1 Gauss limitedLinear 1 Gauss limitedLinear 1 Gauss linear
laplacianSchemes	default	Gauss linear corrected
interpolationSchemes	default	linear
snGradSchemes	default	corrected

Table 3: Summary of numerical schemes used in the simulation.

Numerical Solvers: The Table 4 below summarizes the solvers used for each variable:

Variable	Solver	Tolerance	relTol	Additional Info
rho.*	diagonal	10^{-9}	0	-
(p pFinal)	GAMG	10^{-6}	0.1	Smoother: Gauss-Seidel
(U k epsilon h)*	PBiCGStab	10^{-6}	0	Preconditioner: DILU
(Yi O2 N2 H2O).*	PBiCGStab	10^{-6}	0	Preconditioner: DILU

Table 4: fvSolution solver configurations.

Turbulence, Physics and Physical Property Models: The simulation was performed using the Reynolds-Averaged Simulation (RAS) approach with the kEpsilon turbulence model.

The physical properties of the mixture are modeled using the `hePsiThermo` framework, with the following configuration:

- Thermodynamic Model: `hePsiThermo`, suitable for compressible flows.
- Mixture Type: `multicomponentMixture`, allowing for multiple species interactions.
- Transport Properties: `sutherland` law for dynamic viscosity.
- Thermodynamic Properties: `janaf` polynomials for specific heat capacity and enthalpy calculations.
- Energy Equation: `sensibleEnthalpy`, focusing on the sensible portion of the enthalpy.
- Equation of State: `perfectGas`, assuming ideal gas behavior.
- Species Management: `specie`, defining chemical composition.

The default species is nitrogen (N_2), and the liquid phase includes n-heptane (C_7H_{16}).

Gravity is oriented along $(0, -9.81, 0)$, incorporating buoyancy effects.

Chemistry and Reaction: The simulation includes n-heptane (C_7H_{16}) combustion, utilizing the Chemkin library converted into OpenFOAM-compatible files. The primary combustion reaction is modeled as:



The Partially Stirred Reactor (PaSR) model governs the combustion process. The chemistry solver is `seulex` with $\text{absTol} = 10^{-8}$ and $\text{relTol} = 0.1$. The air composition is modeled as 21% O_2 and 79% N_2 by volume.

Injection Model: The injection process is simulated using the `reactingCloud` approach with the following parameters:

- Outer diameter of injection cone: $d_{\text{outer}} = 1.9 \times 10^{-4} \text{ m}$.
- Injection rate: 200,000 parcels per second.
- Injection profile: Half-sine behavior, illustrated in Figure 3.
- Breakup model: ReitzDiwakar.
- Injected fuel: 100 mg of n-heptane (C_7H_{16}) over 0.1 s.
- Injector position: $(x, y, z) = (0, -0.295, 0)$, oriented in the positive y -direction.

The phase change process uses the `enthalpyDifference` approach, accounting for energy exchange during evaporation. Surface-film interactions are disabled.

2.2.2 Cold Case

The cold case provides a simplified precursor simulation, primarily to initialize the flow field. This phase avoids combustion and Lagrangian tracking, significantly reducing computational cost. The Courant number is increased to 1 for faster computation, with a final time set to $t = 0.05 \text{ s}$. The same mesh, system files, and constants as the hot case (subsubsection 2.2.1) are used, but chemistry and spray modeling are disabled. Initial conditions are detailed in subsubsection 2.3.1.

2.3. Boundary Conditions

2.3.1 Cold Case

Table 5 provides a comprehensive summary of all boundary conditions applied in the cold case prerunner simulation.

Variable	Inlet	Outlet	Walls	InternalField
U	fixedValue (0 11 0)	zeroGradient	noSlip	uniform (0 0 0)
p	zeroGradient	waveTransmissive	zeroGradient	uniform 101325 Pa
T	fixedValue (900 K)	zeroGradient	zeroGradient	uniform 800 K
k	turbulentIntensityKineticEnergyInlet (5%)	zeroGradient	kqRWallFunction	uniform 0.375 m ² /s
ϵ	turbulentMixingLengthDissipationRateInlet (0.02m)	zeroGradient	epsilonWallFunction	uniform 2.0 m ² /s ³
α_t	calculated	calculated	alphatWallFunction	uniform 0
ν_t	calculated	calculated	nutkWallFunction	uniform 0
O ₂	fixedValue (0.233)	inletOutlet (0.233)	zeroGradient	uniform 0.233
N ₂	fixedValue (0.766)	inletOutlet (0.766)	zeroGradient	uniform 0.766
Ydefault	inletOutlet (0)	inletOutlet (0)	zeroGradient	uniform 0

Table 5: Boundary conditions including internal field values.

2.3.2 Hot Case

For the hot case, the boundary conditions are mapped onto the test case using the `mapFieldsDict` utility from `hopperEmptying` in `incompressibleFluid`.

Figures 4 and 5 show the velocity (U), pressure (p), and temperature (T) fields for the precursor simulation at the final iteration $t = 0.05 \text{ s}$. The fields are visualized on two different planes: the xy -plane and the zx -plane.

2.4. Post-Processing

In addition to verifying solution convergence, the following key quantities must be computed and analyzed at specific time instances: $t = \{0.02, 0.05, 0.08\}$. These time points are particularly interesting due to the significant flow phenomena occurring during the simulation.

At $t = 0.02 \text{ s}$, the fuel injection has progressed significantly, and the initial stages of combustion are observed. This marks the onset of high-temperature regions and the generation of turbulence as the fuel-air mixture interacts with the surrounding flow.

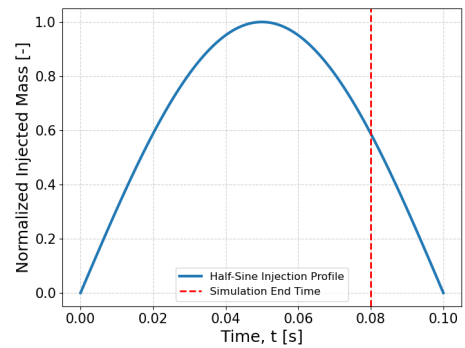


Figure 3: Injector schematic illustrating the fuel flow profile.

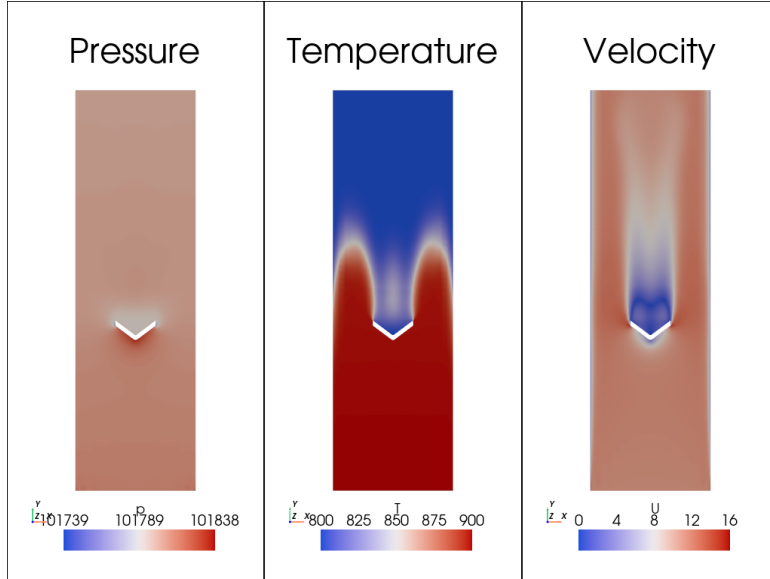


Figure 4: Initial Condition Hot case: Velocity, pressure, and temperature fields on the xy -plane at $t = 0.05s$.

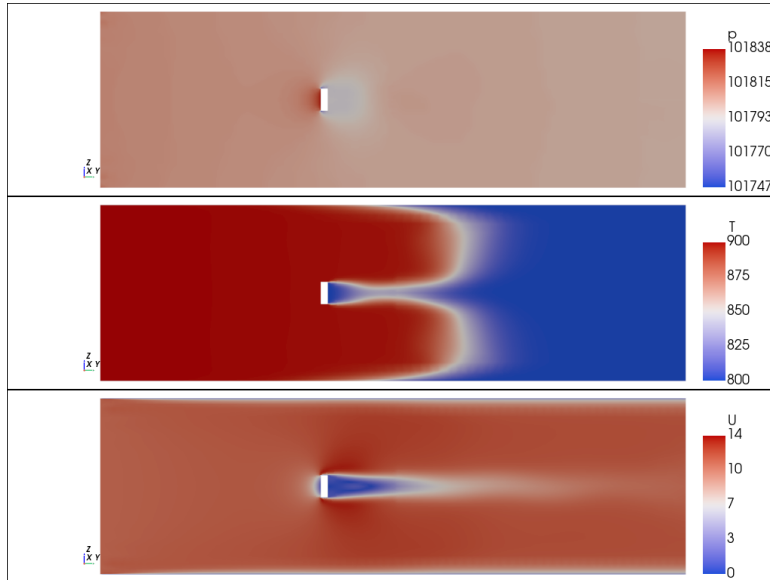


Figure 5: Initial Condition Hot case: Velocity, pressure, and temperature fields on the zx -plane at $t = 0.05s$.

At $t = 0.05s$, the injector operates at its peak performance and the hot combustion gases encounter the V-shaped splitter. This interaction induces complex flow dynamics, including recirculation zones and enhanced mixing due to the deflection and redirection of the flow. The turbulence levels increase substantially in these regions, promoting further mixing.

Finally, at $t = 0.08s$, which represents the end of the simulation, the combusted gases begin to mix extensively downstream of the splitter. This stage highlights the transition toward a more homogeneous mixture, which is crucial for evaluating the combustor's performance and the effectiveness of the mixing process.

These time instances provide a comprehensive understanding of the flow evolution, combustion dynamics, and the role of geometry in enhancing fuel-air mixing.

The primary flow features should be visualized and analyzed, including:

- Velocity field with streamlines.
- Pressure distribution.
- Temperature distribution.

- Heat release rate (\dot{Q}).
- Turbulent kinetic energy.
- Evaporation rate of C₇H₁₆.

To further investigate the combustion characteristics, the air-fuel mixture distribution is analyzed by extracting:

- **Iso-surfaces** corresponding to the stoichiometric air-fuel (A/F) ratio, which delineate the regions where combustion is most efficient.
- The **temporal evolution** of the average pressure and temperature at both the inlet and outlet boundaries, providing an overview of how the system evolves over time and ensuring that boundary conditions remain physically consistent.

Since fuel injection and atomization play a key role in the overall behavior of the system, an analysis of the spray and Lagrangian particle cloud is also performed. This includes:

- The **evolution of parcel size** over time, which helps track fuel atomization and droplet breakup processes.
- **Visualizations of cloud diffusion**, illustrating how the fuel disperses within the combustion chamber and interacts with the surrounding airflow.

All quantities are extracted on the *xy* and *yz* planes, as illustrated in Figure 6. Post-processing is performed using **ParaView** and **Python scripts** to ensure consistency and reproducibility.

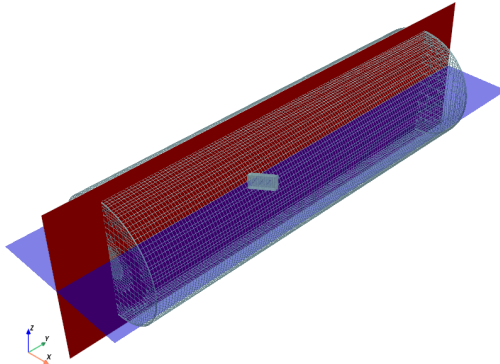


Figure 6: Visualization planes: *xy* (blue) and *yz* (red).

Calculation of the Stoichiometric Air-Fuel Ratio

The combustion of n-heptane is modeled by the following reaction Equation 1

The molar masses of the reactants are:

- Molar mass of C₇H₁₆:

$$M_{\text{C}_7\text{H}_{16}} = (7 \times 12.01) + (16 \times 1.008) = 100.204 \text{ g/mol}$$

- Molar mass of O₂:

$$M_{\text{O}_2} = 32.00 \text{ g/mol}$$

From the reaction stoichiometry, 1 mole of C₇H₁₆ reacts with 11 moles of O₂. Therefore, the mass of oxygen required per kg of n-heptane is:

$$\frac{11 \times M_{\text{O}_2}}{M_{\text{C}_7\text{H}_{16}}} = \frac{11 \times 32.00}{100.204} = 3.515 \text{ kg O}_2/\text{kg C}_7\text{H}_{16} \quad (2)$$

Since air is modeled as containing 23.3% oxygen by mass, the total air mass required is:

$$\frac{3.515}{0.233} = 15.09 \text{ kg air/kg C}_7\text{H}_{16} \quad (3)$$

Thus, the stoichiometric air-fuel (A/F) ratio for n-heptane is:

$$A/F = 15.09 \text{ kg air/kg C}_7\text{H}_{16} \quad (4)$$

Accordingly, iso-surfaces are extracted at an A/F ratio of 15.08.

3. Discussion of the Results

In this subsection, the results of the CFD simulation are analyzed. The discussion begins with the assessment of residual convergence, followed by an in-depth examination of key physical quantities. The analysis then proceeds to the evaluation of Lagrangian spray modeling and concludes with the combustion characteristics.

The simulation was executed on a multi-core system utilizing six processing cores. The total runtime was approximately 12 hours.

3.1. Residual and Convergence Analysis

Assessing the convergence of residuals over time is essential to ensure numerical stability and accuracy. Figure 7 illustrates the residual evolution for different governing equations. The residuals for turbulent kinetic energy (k), dissipation rate (ϵ), and enthalpy (h) exhibit a smooth decline, indicating satisfactory convergence. The pressure residual (p) starts at a relatively high value but steadily decreases throughout the simulation.

However, a critical issue arises in the velocity residuals, which return NaN values during the computation. This anomaly is likely attributed to the deactivation of the momentum predictor. When the momentum predictor is enabled, residuals remain finite, yet instability persists in the early stages, suggesting potential numerical challenges in the solution process. This behavior indicates that further investigation is necessary, particularly in the treatment of pressure-velocity coupling and the numerical schemes employed.

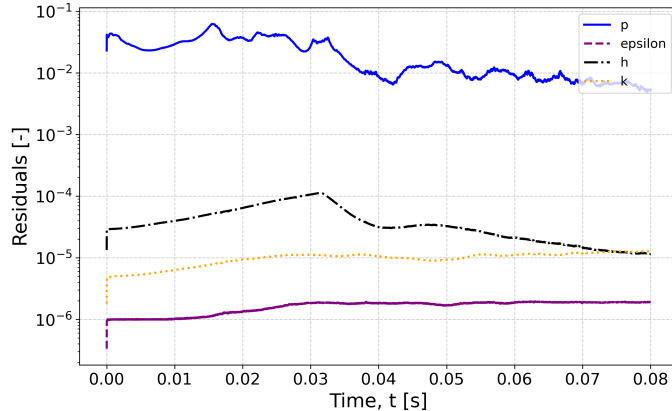


Figure 7: Residual convergence over time for different quantities.

3.2. Key Quantities Analysis

Velocity Field Analysis

Figure 9, Figure 10, and Figure 8c illustrate the temporal evolution of the velocity field within the combustor geometry, highlighting the development and mixing of jet structures over time. The streamlines in Figure 8 are focused around the V-shaped splitter to analyze the behavior of the velocity field as it interacts with this obstacle.

At the initial time instance (Figure 9), the flow remains relatively stable, carrying over from the precursor simulation. Combustion effects are not yet dominant, except in the vicinity of the fuel injection zone, where localized changes are visible due to the mixing and initial reaction stages.

As the simulation progresses to $t = 0.05 \text{ s}$ (Figure 10), the hot combustion gases reach the splitter, where

they are deflected and accelerated. At this stage, the injection process operates at its peak according to the injection profile shown in Figure 3. The interaction with the splitter enhances turbulence and begins to establish recirculation zones, promoting increased mixing downstream.

By $t = 0.08$ s (Figure 8c), the effect of the splitter becomes highly pronounced. The splitter induces a strong recirculation zone that significantly enhances mixing. This phenomenon is further supported by the visualization of turbulent kinetic energy (Figure 13), where k reaches its maximum value, indicating intense turbulence. This turbulence is beneficial for maximizing the efficiency of the combustion process, ensuring better mixing and fuel utilization.

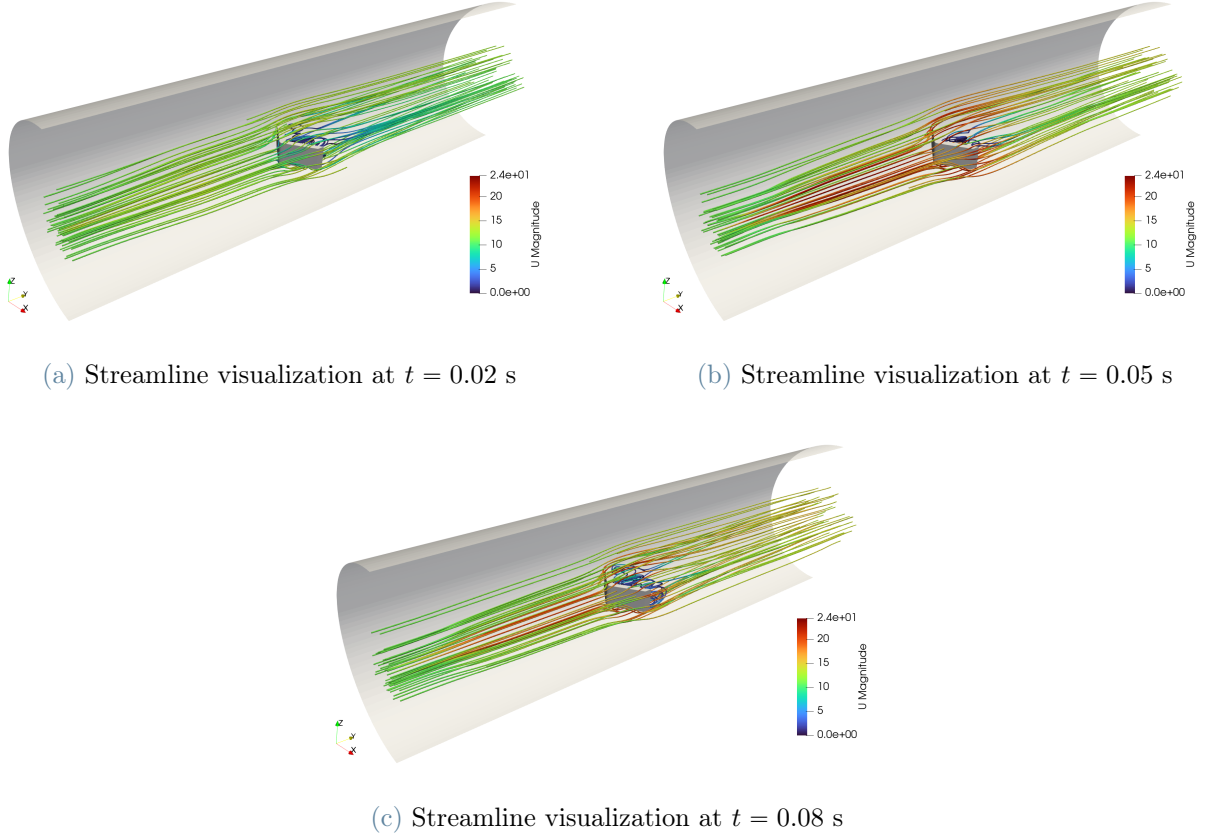


Figure 8: Time evolution of the velocity field, illustrating the development of jet structures and mixing dynamics at different time instances.

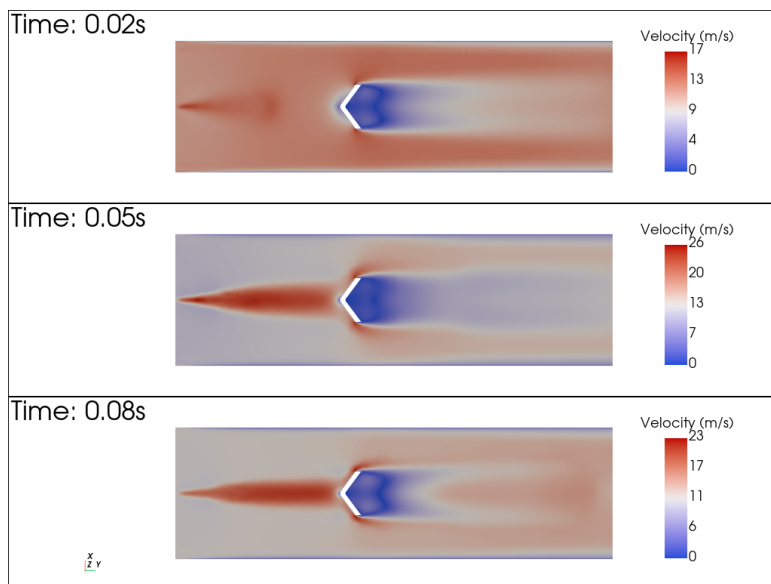


Figure 9: Velocity field visualization in the x - y plane.

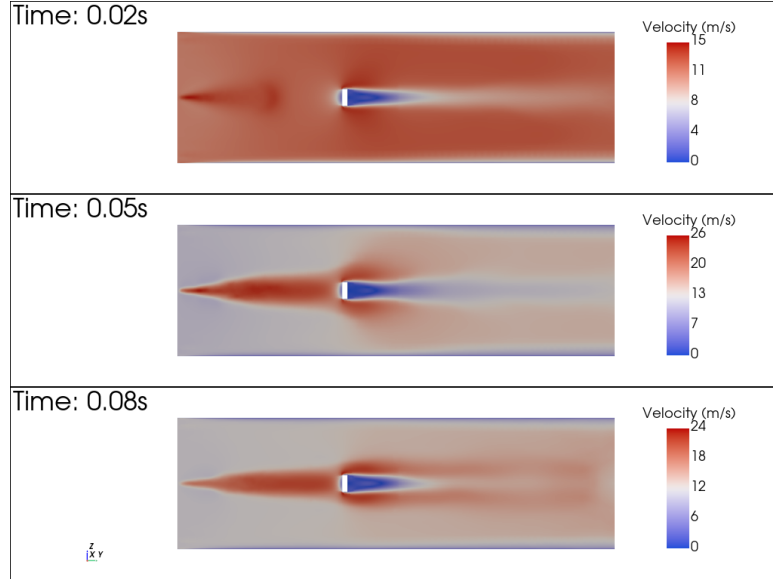


Figure 10: Velocity field visualization in the z - x plane.

Mach Number Distribution

The evolution of the Mach number, shown in Figure 11 and Figure 12, follows the expected trends of the velocity field. Notably, the entire domain remains within the subsonic regime, confirming that compressibility effects are minimal.

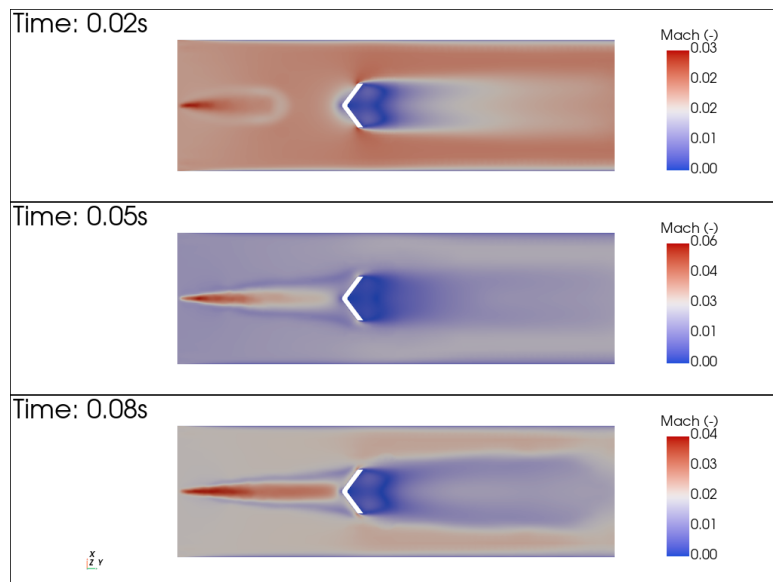


Figure 11: Mach number distribution in the x - y plane at different time instances.

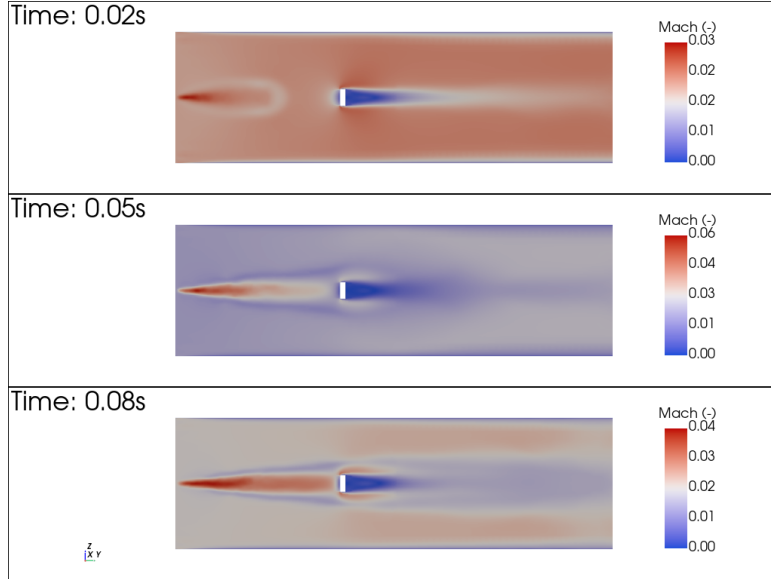


Figure 12: Mach number distribution in the z - x plane at different time instances.

Turbulent Kinetic Energy (TKE) Analysis

Turbulent kinetic energy (TKE), defined as $k = \frac{1}{2} (\overline{u'^2} + \overline{v'^2} + \overline{w'^2})$, represents the energy per unit mass contained in the fluctuating velocity components of the flow. It is a key indicator of turbulence intensity, which is critical for understanding mixing efficiency and the overall flow behavior in reactive systems. Figure 13 and Figure 14 illustrate the TKE distribution in the computational domain at different time instances. Regions of high TKE are concentrated near shear layers, where velocity gradients are sharp, and recirculation zones induced by the V-shaped splitter. These regions are the primary sites of turbulence generation due to the interaction between the high-speed jet and the surrounding slower-moving or recirculating flow.

The range of TKE values provides critical insights into the flow dynamics:

- Low TKE ($k < 10 \text{ m}^2/\text{s}^2$): Indicates laminar-like or weakly turbulent regions with minimal mixing.
- Moderate TKE ($10 \leq k < 40 \text{ m}^2/\text{s}^2$): Represents regions with active mixing, typically in shear layers or downstream of the splitter.
- High TKE ($k \geq 40 \text{ m}^2/\text{s}^2$): Indicates intense turbulence, primarily near recirculation zones or areas with strong velocity gradients, like near the splitter.

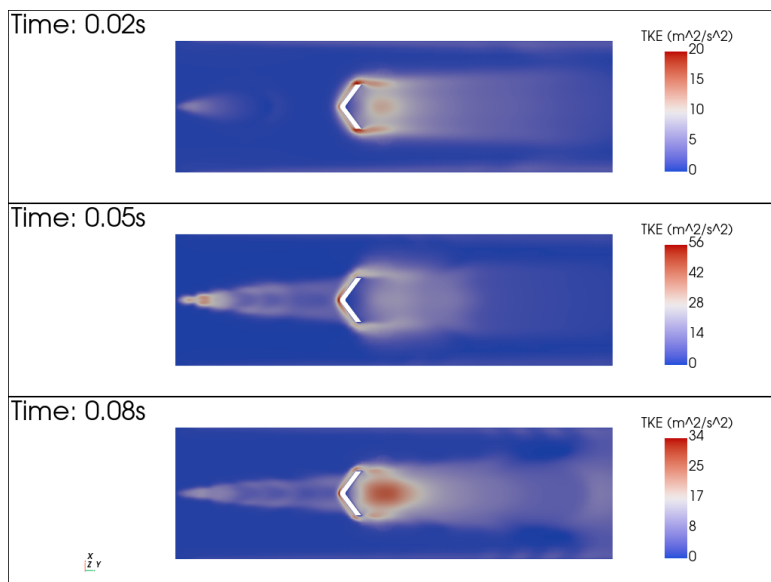


Figure 13: TKE distribution in the xy plane at different time instances.

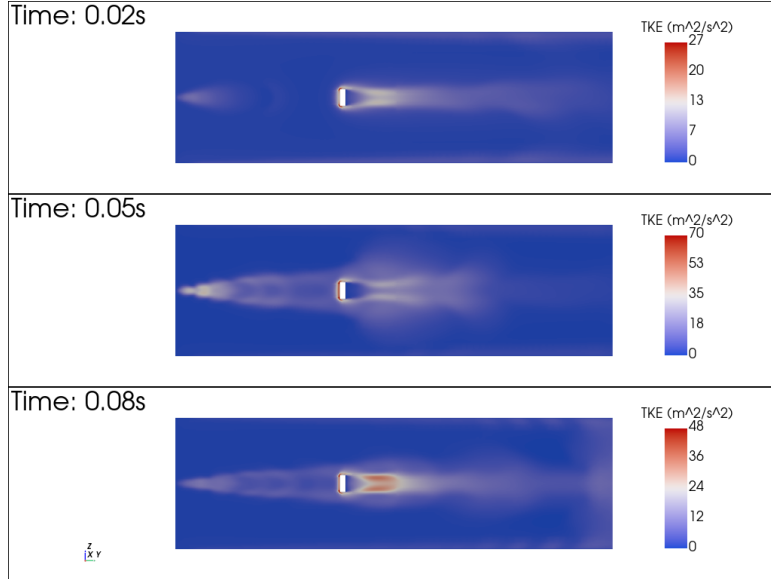


Figure 14: TKE distribution in the yz plane at different time instances.

Pressure Field Analysis

Figure 15 and Figure 16 illustrate the pressure contours over time. High-pressure zones upstream of the V-shaped splitter result from compression effects, while downstream regions exhibit low-pressure recirculation due to flow separation. The symmetry of the pressure field about the central axis validates the numerical results. Over time, the upstream pressure intensifies as the jet interacts with the splitter, and downstream low-pressure zones stabilize, promoting turbulence and efficient mixing.

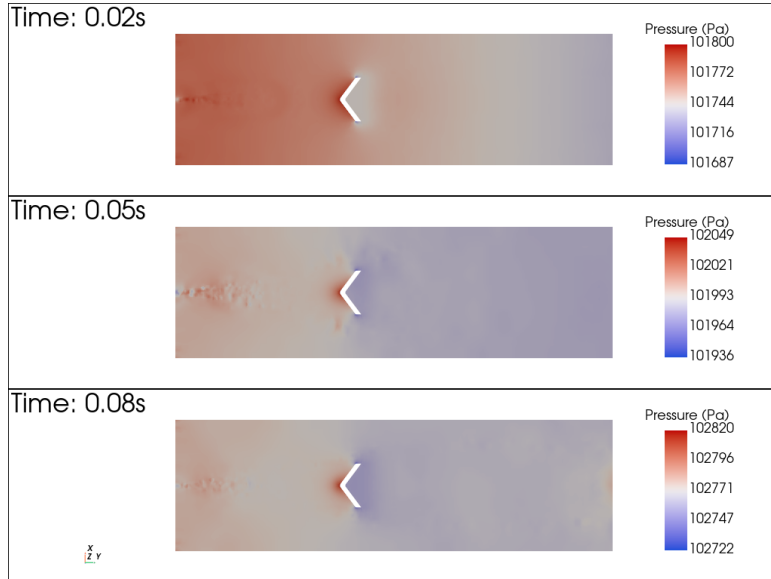


Figure 15: Pressure distribution in the zy plane at different time instances.

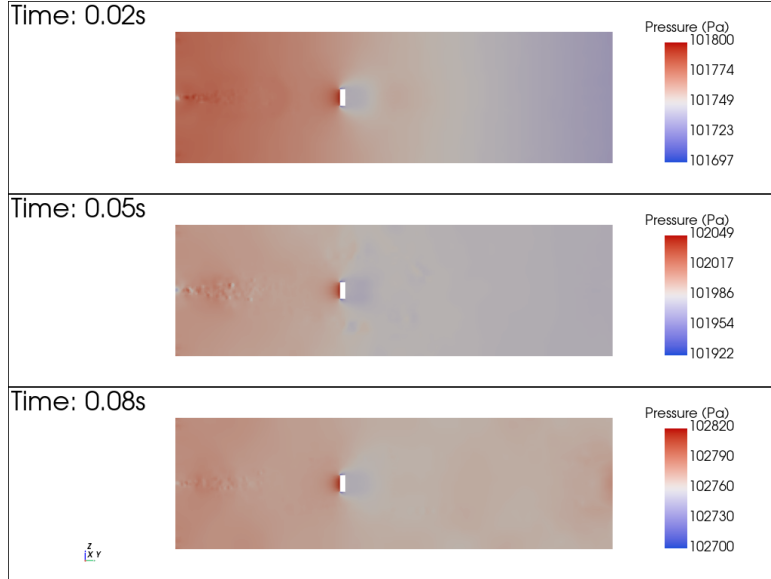


Figure 16: Pressure distribution in the yz plane at different time instances.

3.3. Lagrangian Particles and Spray

Spray Cloud

The evolution of Lagrangian particles within the spray is analyzed in Figure 17. At the initial stages, the particles are concentrated near the injection point, forming a dense core. As time progresses, the spray expands and disperses due to interactions with the surrounding turbulent structures, eventually initiating combustion. The injection profile, shown in Figure 3, results in a peak at $t = 0.05$ s. The parcels are represented as spheres, with their diameter scaled according to their actual size and color-coded based on their temperature.

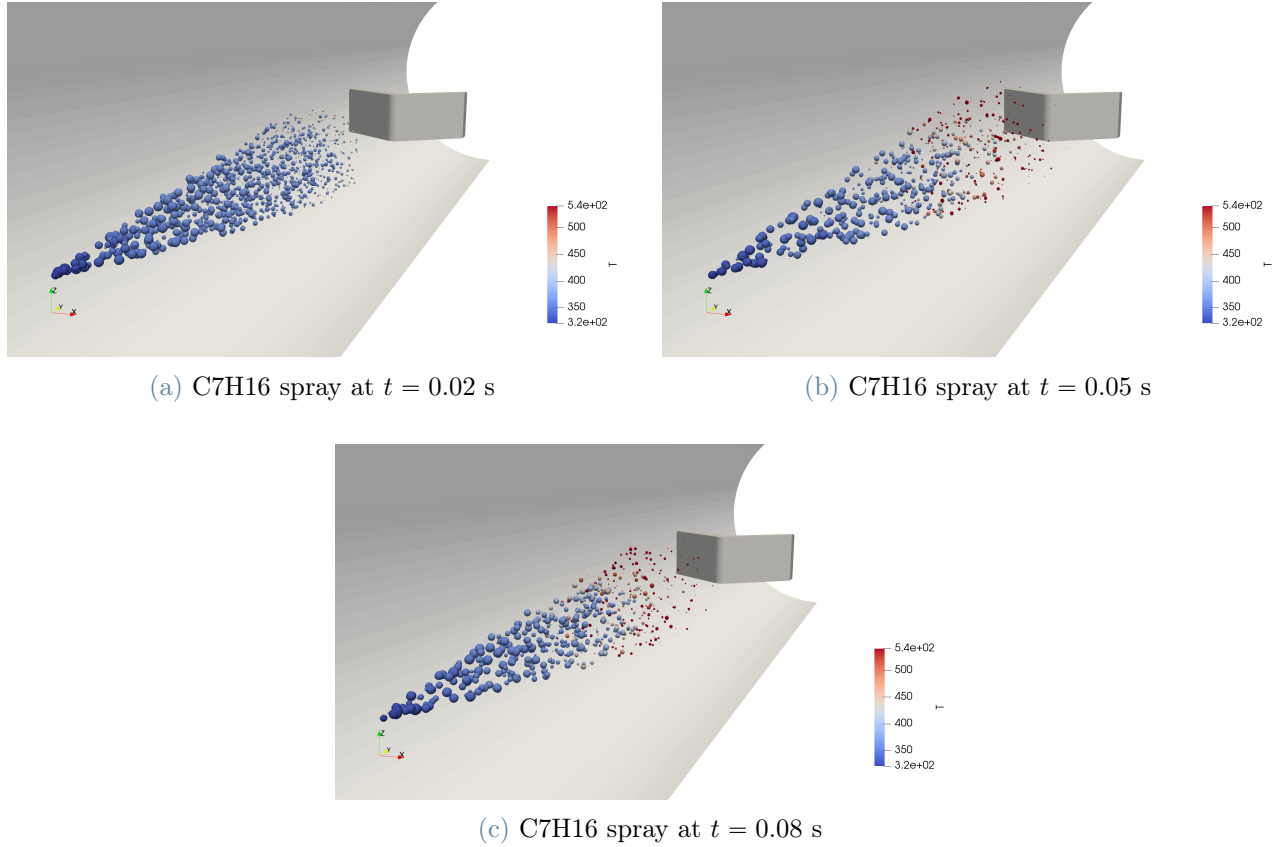


Figure 17: Time evolution of the air-fuel stoichiometric iso-surface

Parcel Size Distribution

Figure 18 shows the evolution of parcel diameters at $t = 0.02\text{ s}$, 0.05 s , and 0.08 s . Initially, the distribution peaks around 50 microns, reflecting the spray injection. Over time, the diameter range broadens due to breakup processes, and larger parcels decrease as vaporization progresses. By $t = 0.08\text{ s}$, the distribution becomes more uniform, indicating effective atomization, improved mixing and high vaporization due to combustion.

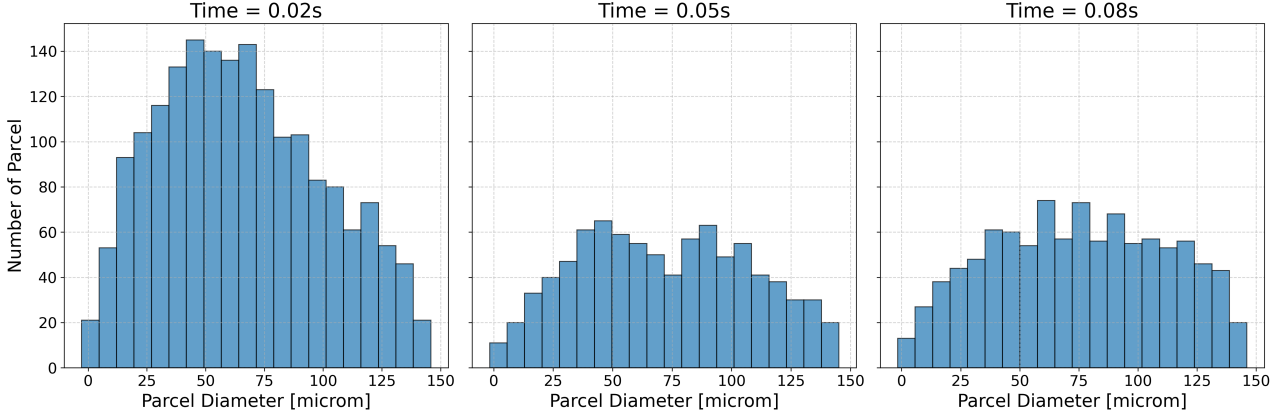


Figure 18: Histogram of parcel diameters at different time instances.

Fuel Vapor Distribution

To analyze the vaporization and mixing processes, Figure 19 and Figure 20 illustrate the vaporized C7H16 mass fraction. Initially, before reaching the splitter, the fuel is concentrated along the central axis. During the early stages, the fuel fraction increases in this region due to continuous injection. As combustion progresses, the fuel is consumed, and by $t = 0.08\text{ s}$, the concentration begins to decrease. Radial diffusion effects become noticeable near the splitter, induced by recirculation zones. The combined impact of combustion and enhanced mixing due to the V-shaped geometry results in a more uniform vapor fuel distribution.

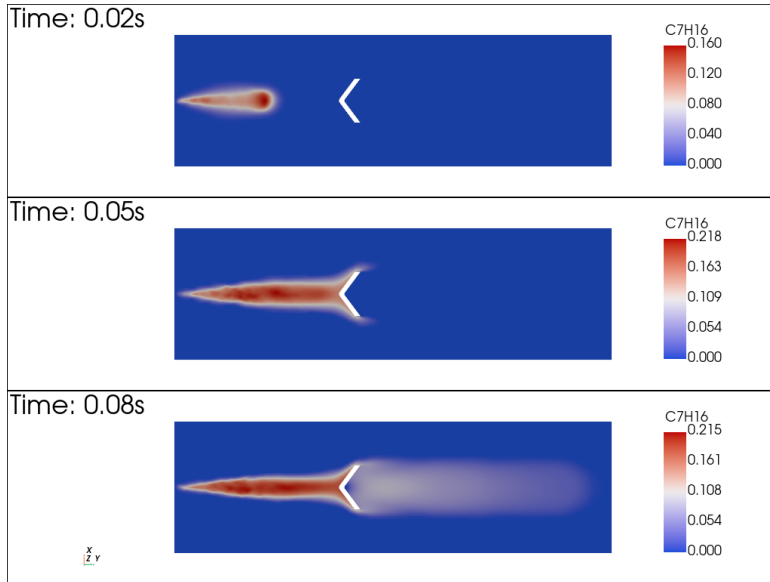


Figure 19: Vaporized C7H16 mass fraction in the xy -plane, illustrating fuel distribution at different stages.

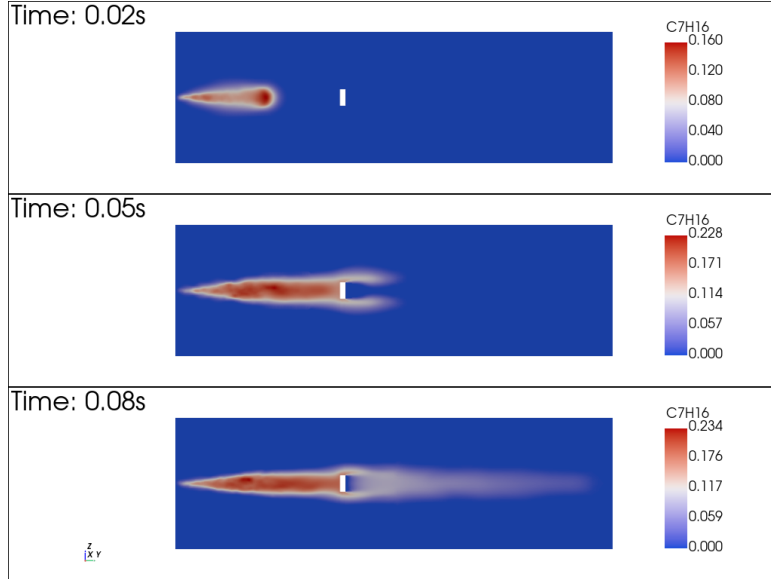


Figure 20: Vaporized C7H16 mass fraction in the yz -plane, highlighting the fuel diffusion along the axial direction.

3.4. Combustion

The impact of combustion on the simulation is analyzed, starting with the visualization of the temperature field, followed by the heat release rate (Qdot) distribution and the evolution of the flame front.

Temperature Field

Figures Figure 21 and Figure 22 show temperature slices at $t = 0.02$ s, $t = 0.05$ s, and $t = 0.08$ s on the planes xy and yz . These visualizations illustrate the thermal effects induced by combustion and provide insights into the spatial distribution of heat within the domain.

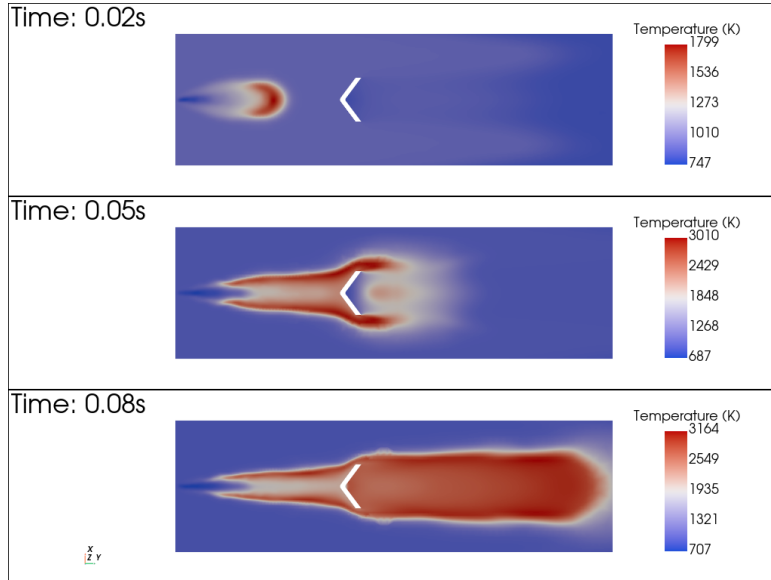


Figure 21: Temperature distribution in the xy -plane at different time instances.

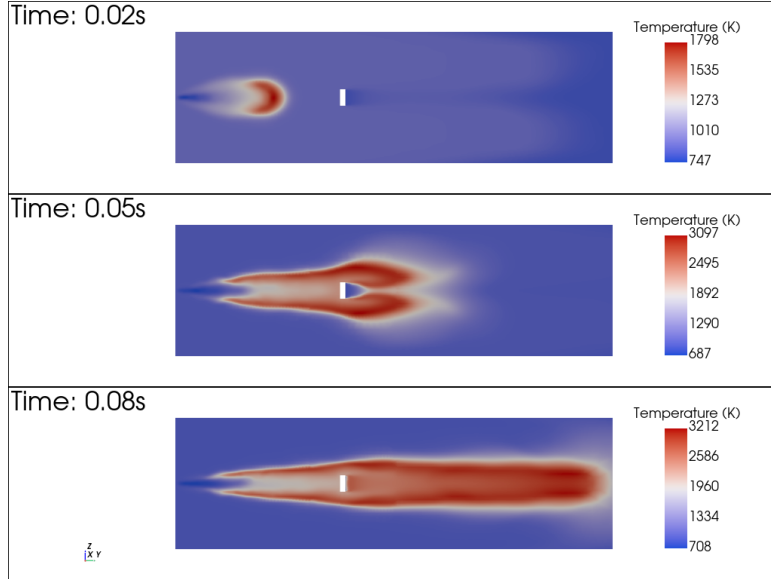


Figure 22: Temperature distribution in the yz -plane at different time instances.

Heat Transfer

The heat release rate (\dot{Q}) is a crucial parameter for evaluating combustion, as it represents the energy transfer resulting from chemical reactions. High \dot{Q} regions indicate areas of intense combustion activity, effectively highlighting the flame front.

Figures Figure 23 and Figure 24 depict the \dot{Q} distribution at different time steps. Intense combustion is observed near the injection point, indicating a stoichiometric combustion zone, as further confirmed by Figure 25. At $t = 0.08$ s, it is particularly noteworthy that combustion occurs also downstream of the splitter, reflecting the sustained reaction process.

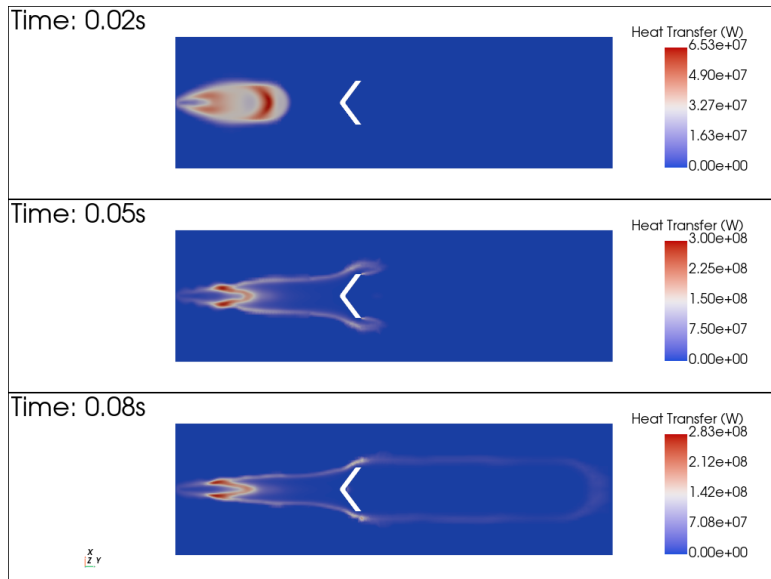


Figure 23: Heat release rate (Qdot) distribution in the xy -plane at different time instances.

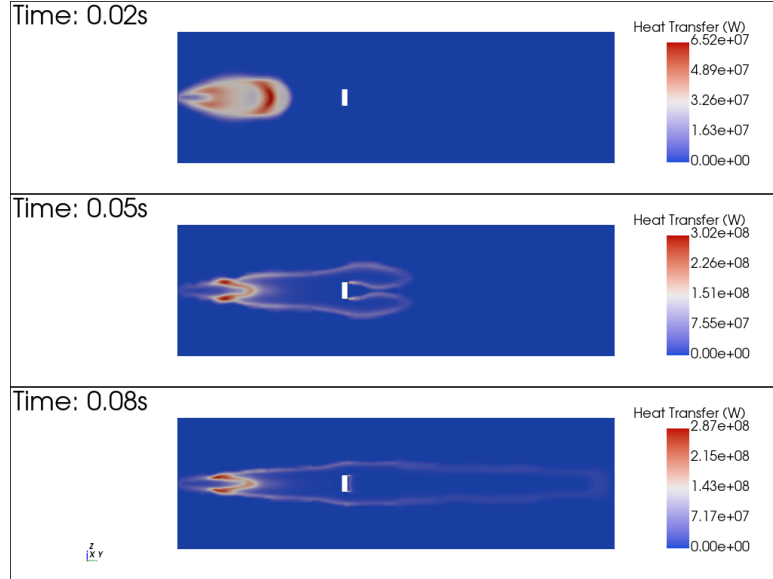


Figure 24: Heat release rate (Qdot) distribution in the yz -plane at different time instances.

A/F stoichiometric iso-surface

A clearer definition of the flame front is provided by the air-fuel (A/F) iso-surface corresponding to the stoichiometric mixture ratio, shown in Figure 25. This iso-surface effectively visualizes the evolution of the reaction zone over time, highlighting the spatial propagation of the flame front.

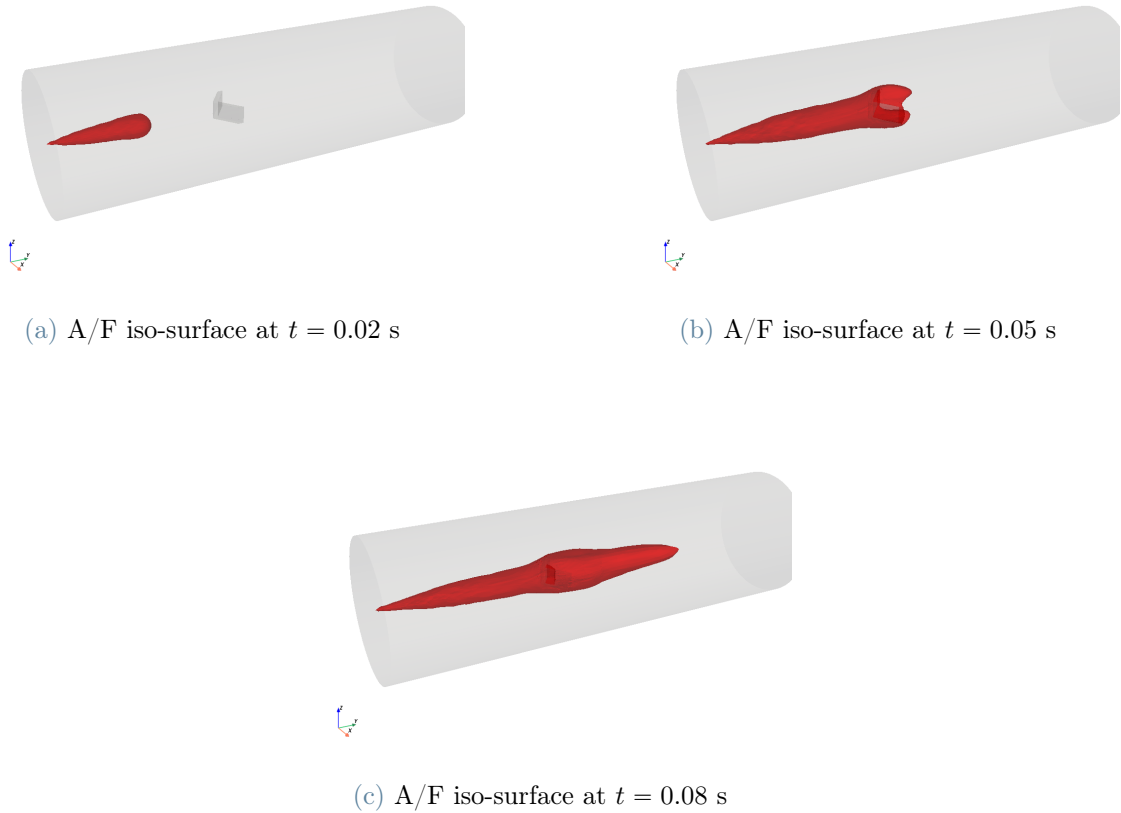


Figure 25: Time evolution of the air-fuel stoichiometric iso-surface, depicting the propagation of the flame front at different time instances.

Chemical Species Concentration

Figure 26 illustrates the concentration of key chemical species (O_2 , C_7H_{16} , and CO_2) over time. Nitrogen (N_2) was excluded from the plot as it is the dominant species (always over 70%), allowing better visualization of the combustion process.

As expected, oxygen (O_2) is initially the most abundant reactant species. Over time, the concentration of C_7H_{16} (fuel) increases due to continuous injection, reacting with and depleting O_2 . This process leads to the formation of combustion byproducts such as CO_2 and H_2O , reflecting the progression and efficiency of the combustion reactions.

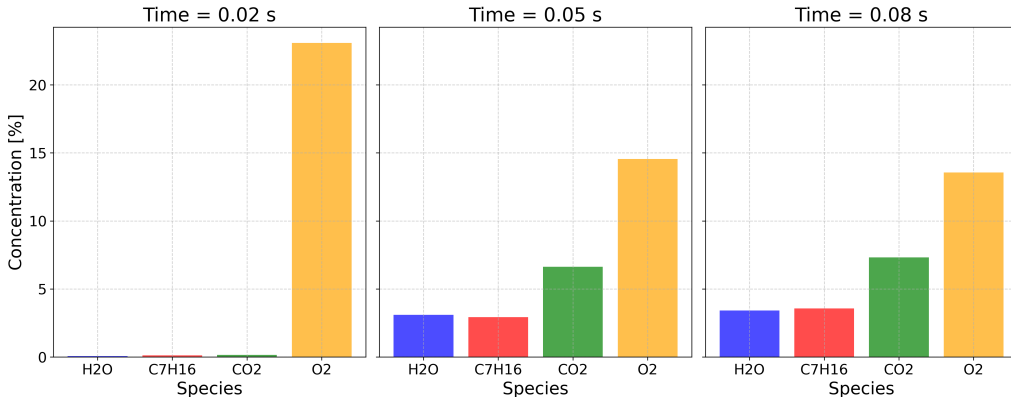
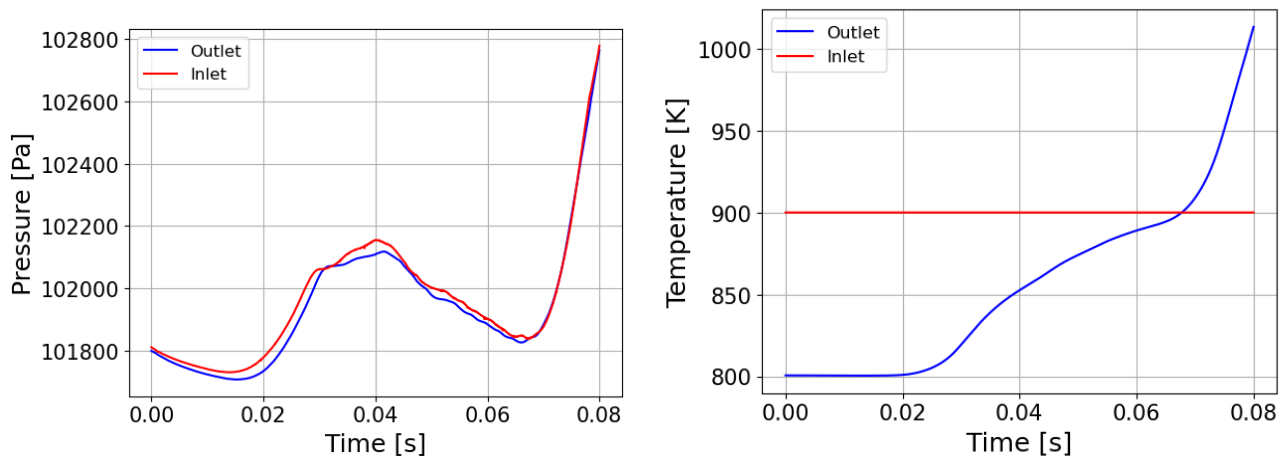


Figure 26: Concentration of selected chemical species (O_2 , C_7H_{16} , CO_2) at different time steps.

Average temperature and pressure on inlet and outlet patch

The temporal evolution of average pressure and temperature at the inlet and outlet boundaries is shown in Figure 27. At the inlet, a constant temperature of 900 K is maintained, whereas at the outlet, temperature varies dynamically based on the combustion process. The pressure evolution follows a similar trend, with smooth variations due to the imposed waveTransmissive condition, ensuring minimal wave reflections and a physically accurate boundary treatment. Interestingly, the combustion process reduces the static pressure at the outlet, a phenomenon attributed to the expansion of gases and the energy release during combustion.



(a) Pressure evolution over time on inlet and outlet

(b) Temperature evolution over time on inlet and outlet

Figure 27: Comparison of pressure and temperature variations over time at inlet and outlet boundaries.

3.5. Animation

To provide a more comprehensive understanding of the simulation results, animations showcasing the temporal evolution of key flow quantities are available on the author's GitHub repository. These animations effectively illustrate the dynamic behavior of the combustion process and its interaction with the V-shaped splitter.

The repository can be accessed at the following link: https://github.com/sarse024/UniversityCODE/tree/main/CTTP_CFD/5-finalProject/Animation.

4. Final Consideration

This study successfully simulated the combustion process of n-heptane in a three-dimensional combustor geometry using a combination of advanced CFD techniques and post-processing tools. The results provide critical insights into the dynamics of combustion, mixing, and turbulence under complex flow conditions.

The mesh refinement strategy was effective in resolving key regions such as the injection area, the V-shaped splitter, and the downstream wake. Despite some challenges with non-orthogonality and computational constraints, the overall mesh quality ensured a balance between accuracy and efficiency.

The combustion analysis highlighted the importance of turbulence in enhancing fuel-air mixing and reaction efficiency. The V-shaped splitter induced strong recirculation zones and elevated turbulent kinetic energy, which significantly improved mixing downstream. This effect was further validated by the stoichiometric air-fuel iso-surfaces and the heat release rate distribution, showing sustained combustion even beyond the splitter.

The temporal evolution of key quantities, such as velocity, pressure, temperature, and species concentration, revealed critical flow phenomena. The injection profile ensured steady fuel delivery, with combustion byproducts (CO_2 , H_2O) increasing over time while reactants (O_2 , C_7H_{16}) depleted. The reduction in static pressure at the outlet, attributed to gas expansion and heat release, was consistent with expected physical behavior.

While the results demonstrated the model's capability to capture the primary flow and combustion characteristics, some numerical challenges were encountered, such as NaN values in velocity residuals when the momentum predictor was deactivated. These issues underscore the need for further investigation into solver settings and pressure-velocity coupling strategies.

In conclusion, the simulation provided a comprehensive understanding of the combustor's performance, emphasizing the critical role of geometry and turbulence in optimizing combustion processes. Future work could focus on incorporating wall interactions, refining the mesh in non-orthogonal regions, and extending the chemical reaction mechanisms for enhanced accuracy and predictive capability.

References

- [1] Federico Ghioldi. *Laboratory material*. Laboratory material. Computational techniques for thermochemical propulsion, Polimi. 2024.
- [2] Federico Piscaglia. *Lecture notes*. Course notes. Computational techniques for thermochemical propulsion, Polimi. 2024.